Astron. Astrophys. 320, 993–1000 (1997)

ASTRONOMY
AND
ASTROPHYSICS

Fine structure of the X-ray and radio emissions of the quiet solar corona

Arnold O. Benz[1], **Säm Krucker**[1], **Loren W. Acton**[2], **and Tim S. Bastian**[3]

[1] Institute of Astronomy, ETH-Zentrum, CH-8092 Zürich, Switzerland (benz at astro.phys.ethz.ch)
[2] Physics Department, Montana State University, Bozeman, Montana 59717, USA
[3] NRAO, P.O. Box 0, Socorro, NM 87801, USA

Received 10 July 1996 / Accepted 27 September 1996

Abstract. Two deep soft X-ray exposures of a quiet region on the Sun were made with the SXT telescope on board the *Yohkoh* satellite on 20 Feb 1995. We report on the spatial X-ray fine structure. Regions of enhanced X-ray emission, more than two orders of magnitude fainter than previously reported X-ray bright points, are loosely associated with bipolar regions in the magnetic network. The power spectrum of quiet X-ray images at small spatial scales is similar to that of active regions, but exhibits a kink at a scale of $\approx 25,000$ km, possibly connected to the supergranular structure. The spatial X-ray structures in the time averaged image amount to an rms amplitude which is 6% of the mean value. The X-ray structures correlate with contemporaneous radio maps obtained by the VLA at wavelengths of 1.3, 2.0, and 3.6 cm. The amplitude of the brightness variations in the images increases with radio wavelength, i.e., with increasing height. The cross-correlation coefficient with the absolute magnetic field strength, however, generally decreases with height, consistent with the idea of bipolar regions in the network and of the magnetic field deviating from vertical in the upper chromosphere.

The X-ray observations require an enhanced pressure in the corona above the magnetic network, but suggest similar temperatures. Model calculations show that, under a constant temperature, an rms density increase (relative to that in the cell interior) ranging from about 20% in the chromosphere to 60% in the low corona is sufficient to explain the observed standard deviations due to the spatial structures in radio waves and soft X-rays, respectively.

Key words: Sun: corona; chromosphere; transition region – Sun: X-rays; radio radiation

1. Introduction

The solar corona currently provides the only opportunity to study the spatial structure of the enigmatic heating process of a stellar atmosphere. X-ray and radio observations probe different layers of the upper chromosphere and lower corona and can be combined to constrain the three-dimensional organization of the processes.

Of particular interest for the heating of the corona above quiet regions in the photosphere (to be called 'quiet corona') is the upper chromosphere and transition region. It is a region of a few hundred kilometers where the temperature changes from less than 10^4 K to more than 10^6 K. The transition region is the result of coronal heating taking place above. The energy balance in the upper chromosphere and the transition region is largely controlled by thermal conduction and radiative losses. Thus any change in coronal heating must have an immediate effect on the layers below via conduction. Irradiation and local energy release may constitute additional inputs.

The change from the corona to the chromosphere can be observed in the free-free (thermal electron bremsstrahlung) continuum of radio waves and in soft X-ray spectral lines. High spatial resolution in X-rays has recently become available through the *Yohkoh* satellite and is similar to the resolution of the VLA in radio waves.

An well-known constituent of soft X-ray emission from quiet regions and of coronal holes are soft X-ray bright points (e.g. Golub et al. 1974). They consist of magnetic bipoles, typically 10^4 km in size, with a mean lifetime of 8 hrs. The X-ray bright points and their associated He I absorption in the chromosphere occur primarily above newly emerged bipolar regions and even more frequently in disappearing, or canceling, elements of the network (Harvey 1985).

Full Sun X-ray images are dominated by active region loops, prohibiting long accumulation times. This technical limit has made it difficult in the past to detect the emission of the quiet regions except for the bright points.

The first direct comparison between X-ray bright points and *centimeter radio waves* were made only recently by Nitta et al. (1992). Enhanced radio emission during optically observed coronal brightenings has previously been observed at 20 cm wavelength (Habbal et al. 1986, Habbal & Harvey 1988), at 6 cm (Fu et al. 1987) and more recently at 2 cm (Kundu et al.

Send offprint requests to: A.O. Benz

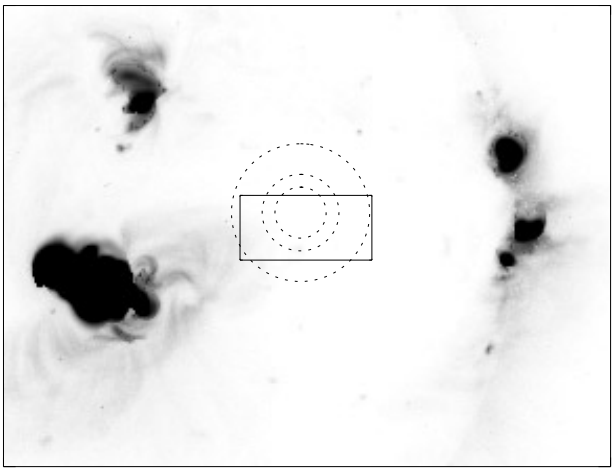

Fig. 1. A large field of the solar soft X-ray emission was observed by Yohkoh/SXT on 1995/02/20 at 23:18 UT in the AlMg filter. Enhanced emission is shown dark. The field of view observed by deep exposures is indicated by a rectangular frame. The field of view (primary beam) of the radio observations made at the VLA is shown by dashed concentric circles increasing in radius for 1.3, 2.0, and 3.6 cm.

1994). The total duration of the radio events is similar to the X-rays. Rapid variations observed in the radio emission suggest that individual loops brighten and fade on time scales of minutes.

A weak correlation between enhanced radio emission and the magnetic network has been noted by Kundu et al. (1988) and Gary & Zirin (1988) at 20 cm. The correlation becomes much better at 6 cm and shorter wavelengths – radiation on these wavelengths originates predominantly in the upper chromosphere with the corona making only a small contribution (Kundu et al. 1979; Gary et al. 1990). Discrete sources in radio maps of the chromospheric network are variable on time scales of a few minutes (Gary & Zirin 1988; Gary et al. 1990) although the overall structure of radio emission is maintained for many hours, consistent with the lifetime of network itself (Bastian, Dulk, & Leblanc 1996).

Here we present long exposures of the quiet corona in soft X-rays. They are sensitive to structure that is more than three orders of magnitude weaker than the previously published X-ray bright points. The spatial structures in soft X-rays are compared to radio maps at 3.6, 2.0 and 1.3 cm, originating mostly from the upper chromosphere and the transition region at altitudes increasing with wavelength. We also compare the X-ray and radio structures to the magnetic network of the photosphere. This paper is limited to the spatial aspects of the observations and of the various correlations. The results of an analysis of temporal variation in the radio and soft X-ray bands will be published separately by Krucker et al. (1997).

2. Observations

A quiet region on the solar disk centered at S3W26 was observed on 20 Feb 1995. The soft X-ray telescope (SXT) on board the *Yohkoh* satellite (Tsuneta et al. 1991) has an effective area of about 0.5 cm^2 (for the filters used) and a spatial resolution (50% of energy flux) of $4''.3$. The SXT observed the target from 20:53-21:34 UT and from 22:30-22:50 UT alternating between the Al.1 filter (5.8-13.2Å) and the AlMg filter (5.8-12.2Å) with exposure times of 15.1 s each. The total accumulation time in each filter was 1560 s during these two intervals. The field of view was restricted to a rectangle of 128 × 64 pixels ($2''.455$ in each dimension), yielding a total size of $314'' \times 157''$. A part of full disk image shown in Fig. 1, taken shortly after this observing sequence, indicates the location of the field of view on the disk and displays the neighboring active region loops. The solar limb goes vertically across the right part of the figure. Active region 7843 is prominently visible near the center of the disk. A smaller active region, 7842, is located at about three arcmin from the east boundary of the field. Nevertheless, high-reaching loops of active regions 7842 and 7843 are projected into the eastern half of the field of view. Most of the analysis concentrates on the first time interval and the western half of the field of view.

The radio observations at the Very Large Array (VLA) were carried out during a longer time interval, lasting from 16:26 until 23:57 UT, to improve the image using Earth rotation aperture synthesis. We observed the three frequencies 8.41, 14.96, and 22.49 GHz to which we refer by the wavelengths 3.6, 2.0 and 1.3 cm, respectively. Each was measured sequentially in two minute intervals interrupted by phase calibration every half an hour. During the time intervals of deep *Yohkoh* integrations, the VLA remained at 2 cm. The net bandwidth observed in each wavelength band was 50 MHz. The array was in C configuration yielding an average synthesized beamwidth (FWHM) of $6''.5 \times 3''.1$, $3''.9 \times 2''.0$, and $2''.9 \times 1''.5$ at 3.6, 2.0, 1.3 cm, respectively.

The reader may here be reminded that interferometers do not measure the absolute flux of the Sun, but brightness variations relative to the mean brightness in the field of view. The field of view of the VLA is determined by the angular response of a single 25m antenna, the primary beam. Its FWHM size is $328''$, $212''$, and $138''$ at 3.6, 2.0, and 1.3 cm, respectively. The fields of view are shown in Fig. 1 by concentric circles increasing in size with wavelength. Since, in the case of solar observing, the antenna sidelobes also fall mostly on the Sun, the brightness of solar observations must be corrected for enhanced antenna efficiency (Bastian et al. 1996).

A full Sun magnetogram is available based on observations with the Kitt Peak vacuum telescope at 15:14-16:09 UT. The original pixel size is $1''.15$.

The positional uncertainty of the X-ray observations are less than the pixel size of $2''.5$. The radio observations are better than $1''$. The position of the magnetogram was corrected for solar rotation. Its uncertainty is dominated by temporal variations rather than pointing accuracy. Thus the uncertainty of the superposition of the different observations is less than the pixel size.

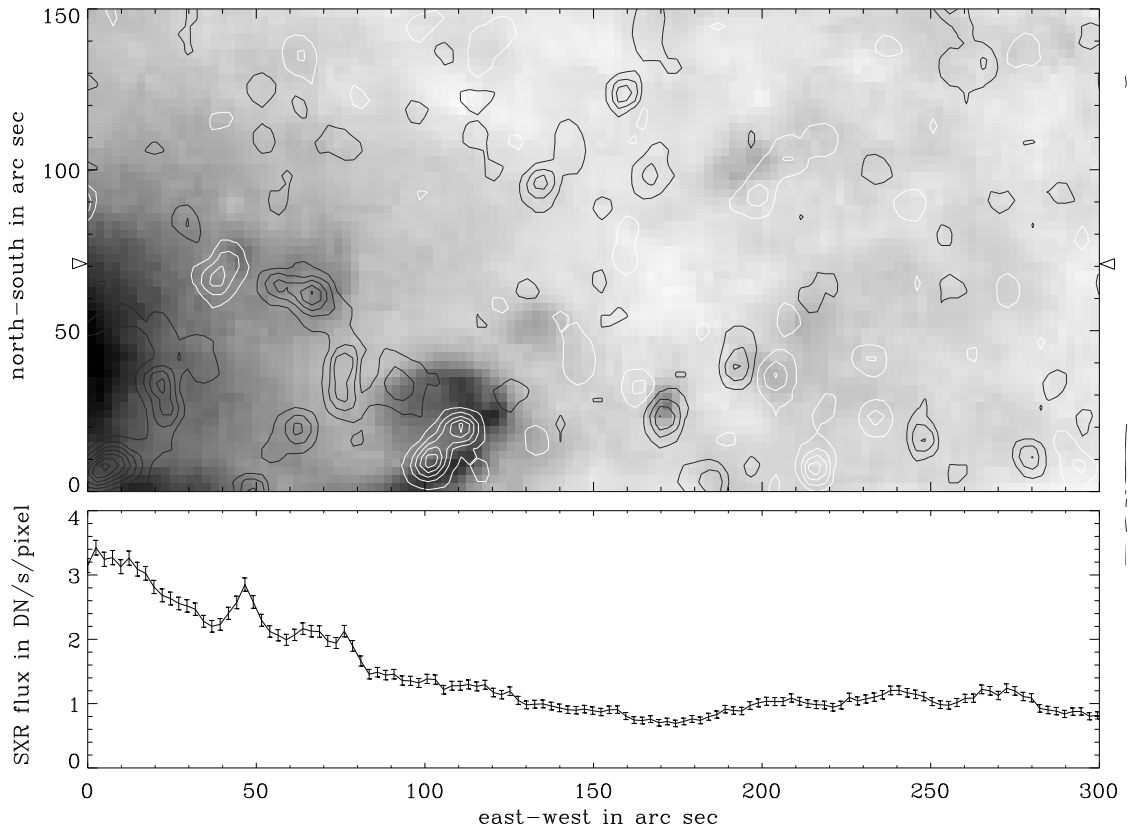

Fig. 2. a Quiet region of the Sun observed in a deep exposure of Yohkoh/SXT on 1995/02/20. The Al.1 filter image is shown in gray scale; enhanced intensity is dark. It was accumulated for an effective time of 785 s between 20:53-21:34 UT. The location of the field of view is shown in Fig. 1. The KPNO magnetogram is overlaid in contours of constant average longitudinal magnetic field strength at the levels $\pm 5, \pm 15, \pm 25$ etc. gauss. Positive values are shown in white, negative ones are black. **b** An East-West cut through the center of the above image (marked by open triangles) displays the soft X-ray flux in units of *Yohkoh* Data Numbers (DN) per second and 2″.455 pixel. One DN corresponds to about 3 photons.

3. Correlations and discussion

3.1. Soft X-rays

Fig. 2 is a soft X-ray image of extremely long exposure resulting from a combination of all data of the Al.1 filter taken during the first time interval. The weak structures of the quiet corona are emphasized by the gray scale. The contours indicating the average longitudinal strength of the magnetic field per resolution element outline the magnetic network in the photosphere and chromosphere having a scale of 20'000 to 50'000 km. The network elements increase in peak strength in the lower left corner, the direction to active region 7842. The pronounced network structure and the highest peak being only 80 gauss indicate that the field of view comprises a section of the photosphere that is completely quiet. In soft X-rays, however, some high reaching coronal loops of the distant active region are projected into the eastern half of the image. They produce a foreground through which the enhanced X-ray structures of the low corona are still visible.

In Fig. 2 the rich X-ray structure of the quiet corona is evident. Although some detail is lost in the image because of the long time-averaging, X-ray loops connecting bipolar magnetic elements are discernible; e.g., at the bottom of the image, just to the left of the middle. Other X-ray features, e.g. at positions 170"/25" and 200"/40", are located between bipolar network elements, suggestive of connecting loops.

The power spectrum of the right half of the X-ray image is presented in Fig. 3a. Each line (column) was transformed and the result averaged over all columns (lines) for an East-West (North-South) spectrum. The spectra decrease with wavenumber k up to $k \approx 1.14$ rad/Mm, where the spectrum becomes constant. This value corresponds to scale sizes of 5500 km (7″.6) and is close to the Nyquist number $k_N = 1/2\Delta$, where Δ is the effective resolution. At higher wavenumbers the spatial resolution of the SXT instrument is increasingly oversampled, and the spectrum is flattened by noise. Thus the soft X-ray observations contain significant structure down to the resolution limit.

The spectrum in Fig. 3a is not a simple power-law. The slope below $k \approx 0.27$ rad/Mm has a power-law index of -1.4±0.2. For $0.27 \lesssim k \lesssim 1.1$ rad/Mm the slope decreases with $k^{-2.7}$. It is similar to k^{-3} reported by Gómez et al. (1993) for active regions. The break point corresponds to a scale of 25'000 km, suggestive of the supergranular scale.

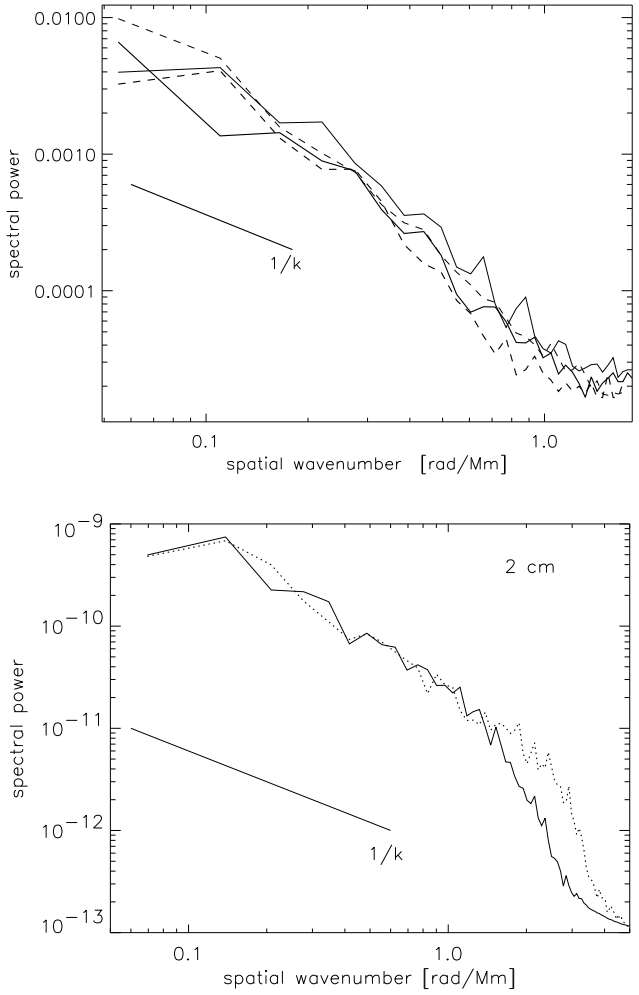

Fig. 3. a Power spectrum of the soft X-ray image. Only the right part of Fig. 2 was selected. The spectra are in one dimension: East-West (solid) and North-South (dotted). The thick curves represent the first time interval, the thin curves the second time interval. **b** Power spectrum of the 2 cm radio image (square of 112"×112" in the primary beam, total observing time). The spectra are in one dimension: East-West (solid) and North-South (dotted).

3.2. Radio waves

The power spectrum of the radio image at 2 cm (Fig. 3b) has a power-law part with an index of -1.8. The low-wavenumber break at 0.143 rad/Mm corresponds to a scale size of 44'000 km. Note the sharp cut-off at high wavenumbers due to the beam size. Contrary to soft X-rays (Fig. 3a) where the spectrum at large wavenumbers is dominated by noise, the radio image does not contain much noise at scales below the beam size. As the beam is narrower in the North-South direction (1$''$.8), the power-law extends to higher wavenumbers than in East-West direction. The difference between North-South and East-West in Fig. 3b clearly demonstrates that structures as small as the resolution limit have been detected in the 2cm image. The existence of fine structure in the 2cm emission of the quiet corona at this small scale is surprising, as radio emissions at 20 cm wavelength, where a considerable fraction is coronal, appear to be resolved at 15$''$ resolution (Gary & Zirin 1988). Radio wave scattering in the solar atmosphere may be the main reason. The observations agree with the ν^{-2}-law of radio wave scattering and a plausible model of the inhomogeneity in the solar atmosphere (Bastian 1994).

Fig. 4 confirms that enhanced radio emission is often, but not always, associated with regions of enhanced magnetic field in the network and vice versa (as was shown by Erskine & Kundu, 1982, at 6 cm). The cross-correlation of the radio intensity with the absolute magnetic flux is significant at all observed wavelengths. Table 1 gives the peak values near zero lag. Peak correlation is often shifted by several arcseconds similar to the X-rays. The cross-correlation is best and peaks closest to zero lag for the short wavelength, originating from the smallest height. The correlation of the radio image with the magnetic field is clearly less than the one found in an old, decayed active region by Gary & Zirin (1988) at 6 cm.

Table 1 also indicates that the 1.3cm and 2.0cm images correlate very well. The 2.0cm and 3.6cm maps correlate well, but are displaced from each other. The correlation between the 1.3cm with 3.6cm maps is less pronounced.

3.3. Cross-correlations

A comparison of X-ray emission and photospheric magnetic field in Fig. 2 indicates that most, but not all, enhanced magnetic field regions are sites of elevated X-ray emission. In the left half of Fig. 2, dominated by the loop-shaped X-ray emission of bipolar regions, the bipolar regions are often at the footpoints of the elongated X-ray brightenings. In the right half of the image the peak of the X-ray emission is also slightly displaced or between bipolar regions, suggesting that the X-ray emission generally originates in magnetic loops rooted in the photospheric region of enhanced average magnetic field.

The two-dimensional cross-correlation of the X-ray emission and the magnetic field is shown in Fig. 5a. The statistical significance of the correlation is determined by a Student's t-test. The degrees of freedom of the statistical problem are given by the number N of independent picture elements of the image with the lower spatial resolution. In all cross-correlations the field was chosen to be $112'' \times 112''$ centered in the upper middle of Fig. 2. The field does not include the projected strong sources in the lower left corner of Fig. 2. For Fig. 5a and an effective resolution of the SXT amounting to 4$''$.3, $N \approx 678$. The test on the observed peak correlation of 0.15 then indicates a significant correlation. It confirms the association of the coronal X-ray emission with enhanced photospheric magnetic field and the magnetic network in general.

The statistical error of the cross-correlation is of the order of $N^{-1/2}\sigma/F$, where F/σ is the signal-to-noise ratio of the noiser data set. The statistical error in Fig. 5a then is 0.01. However, the cross-correlation coefficient is dominated by relatively few intense structures. Therefore, the values given in Table 1 refer to a particular quiet region and may not be general. For this reason, the errors given in Table 1 are not representative.

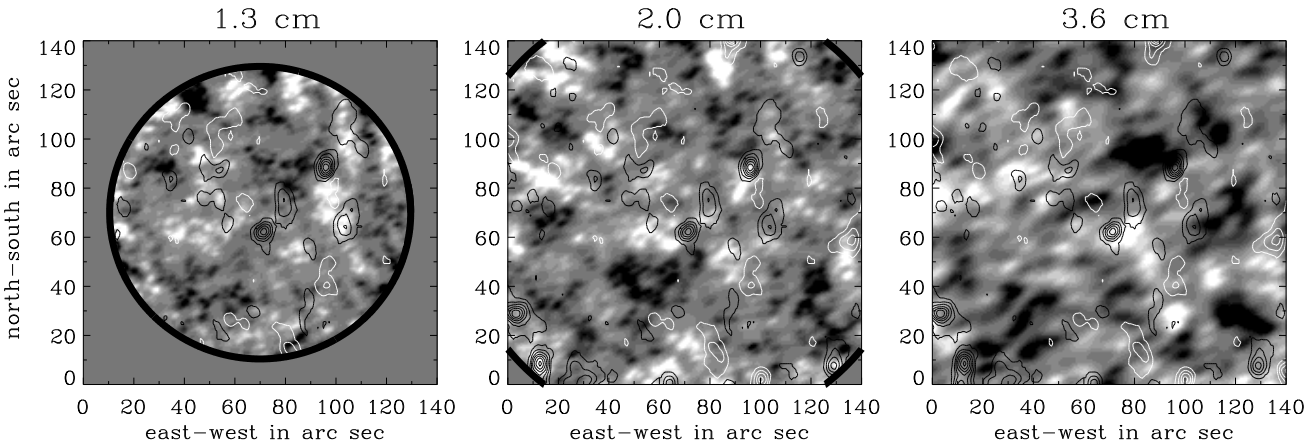

Fig. 4. Radio images of the quiet region observed by the VLA at three different wavelengths in the time interval 16:16-20:40 UT. Brightness indicates enhanced intensity. The KPNO magnetogram is overlaid in contours, white meaning positive flux and black negative flux. The levels shown are ± 10, ± 20, etc. gauss.

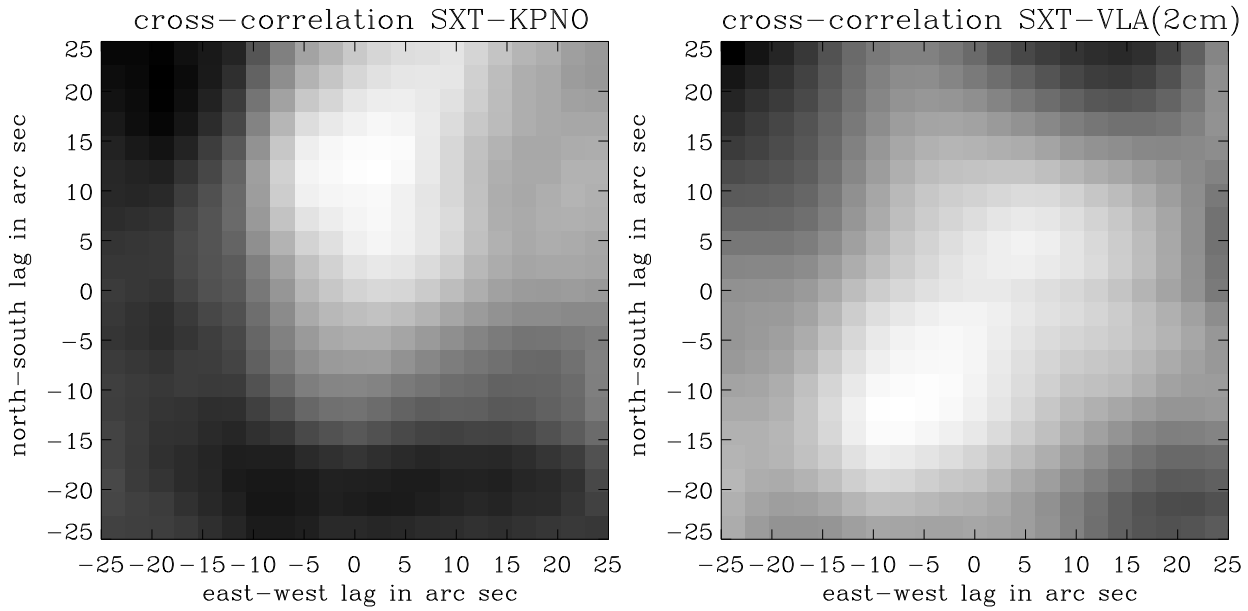

Fig. 5. a The soft X-ray image (right half of Fig. 2 only) was cross-correlated with the magnetogram (absolute value) in two dimensions. The cross-correlation coefficient is shown in gray scale from dark (negative values) to bright (peak value). The step is 2″.455. **b** Two-dimensional cross-correlation of the soft X-ray image with the radio image at 2.0 cm wavelength.

The error in the position of the peak correlation is determined by the spatial resolution and the statistical noise in the two images. This is better than the 0″.1 accuracy with which the shifts have been read out. Note that in Fig. 5a the total displacement of the peak correlation from zero lag is 12″.5. Fig. 2 suggests that this is mainly caused by the X-ray emission originating between the two elements of bipolar regions. Since these individual shifts appear to be random, the strongest elements then dominate the direction of displacement in the cross-correlation. Thus the net shift of peak correlation is the result of a few elements, and the variation from region to region may be much larger than the statistical error.

The cross-correlation of the X-ray image and the simultaneous radio intensity at 2 cm is shown in Fig. 5b. It shows the weakest of all cross-correlations. The correlation peaks at 0.07 is still significant. The peak is displaced by only 6″.5 from zero lag. The small displacement of the peak indicates that the soft X-ray emission and 2cm radio emission are indeed correlated. The correlation seems to have at least two peaks. The second peak, displaced by 14″.5, is even higher. Thus there seem to be two preferred directions of displacement and the correlation is smeared out over many lags, reducing the central peak, which is smaller than the cross-correlation with the magnetogram. An example of the cross-correlation of radio images with the magnetogram

Table 1. Properties of images. The X-ray values are given in Data Numbers (3 photons) per second and pixel and refer to the right part of Fig. 2. The radio values are in degrees kelvin and are calculated from the primary beam image produced only from the data taken in the three-frequency mode. Thus the values for the 3 radio frequencies are based on the same integration time. The errors are discussed in the text.

	VLA 1.3cm wavelength	VLA 2.0cm wavelength	VLA 3.6cm wavelength	SXT Al.1 filter
beam	$2''.9 \times 1''.5$	$3''.9 \times 2''.0$	$6''.5 \times 3''.1$	$4''.3 \times 4''.3$
field of view	$120''$	$180''$	$321''$	$64'' \times 128''$
maximum	1320 K	2930 K	5640 K	2.47 DN/s·pix*
minimum	-1610 K	-2310 K	-5042 K	0.60 DN/s·pix*
standard deviation	290 K	580 K	930 K	0.172 DN/s·pix*
cross-correlation coefficient with				
magnetogram peak value	0.26±0.005	0.27±0.005	0.19±0.005	0.15±0.01*
displacement	$21''.2 \pm 0.1$	$5''.1 \pm 0.1$	$9''.8 \pm 0.1$	$12''.5 \pm 0.1$*
cross-correlation between emissions:				
peak value and displacement				
SXR	-	$0.07/6''.5$	-	-
3.6cm	$0.23/5''.5$	$0.33/11''.5$	-	-
2.0cm	$0.31/1''.7$	-	-	-

* right half of Fig. 2

is shown in Fig. 6. The peak values and peak displacements are given in Table 1.

4. Interpretation

4.1. X-Ray Structures of the quiet corona

Coronal soft X-rays are a combination of free-free radiation and (more importantly in the present case) line emissions. The flux density may be written as an integral over the emitting volume V,

$$S(\lambda) = \frac{1}{4\pi D^2} \int f(\lambda)\eta(T,\lambda)n_e^2 \mathrm{d}V \quad [\mathrm{ergs}^{-1}\mathrm{\AA}^{-1}\mathrm{cm}^{-2}] \,, \quad (1)$$

where $f(\lambda)$ is the filter function of the telescope depending on wavelength λ, η is the emissivity per unit emission measure, and n_e is the electron density. The factors of Eq.(1) have been determined and integrated over the wavelengths observed by the SXT filters (Tsuneta et al. 1991, Fig. 9). The result can be written in the form

$$F = \int r(T)n_e^2 \mathrm{d}V \qquad [\mathrm{photons\ s}^{-1} \cdot \mathrm{pixel}^{-1}] \quad (2)$$

where the integral is along the depth of a pixel. The response function $r(T)$ for the Al.1 filter has a broad peak at $5 \cdot 10^6$ K, is rather flat above, and drops off rapidly below about $2.5 \cdot 10^6$K with a slope of approximately T^4. It is reduced by a factor of one hundred at 10^6 K.

A formal temperature of $1.3 \cdot 10^6$ K results from the ratio of the X-ray counts observed in the two filters. This temperature is a weighted average over the X-ray emitting material. It indicates that most of the emitting plasma is at a temperature in the T^4 regime of the response function. This makes clear that *not much plasma exists in the quiet corona at temperatures above* $1.3 \cdot 10^6$ *K*.

If the kinetic pressure, $n_e k_B T_e$, were constant in the field of view, an enhanced temperature would increase the X-ray intensity observed by SXT as T^2. One may thus expect that regions of enhanced emission were hotter. On the contrary, the observed temperature of bright regions is generally similar or smaller than in the network cells. Therefore, the kinetic pressure must be larger in the X-ray bright regions of the quiet corona. In active regions, a correlation between SXR flux and gas pressure has been found by Yoshida & Tsuneta (1996). To reproduce the observed quiet Sun X-ray structures, the density must be enhanced in the sources above the network.

4.2. Structures in the radio emission

The radio emission of the quiet Sun is generally agreed to be mostly thermal free-free radiation (e.g. Chiuderi Drago et al., 1983). Nevertheless, the radiation is not known well enough to exclude occasional contributions of non-thermal emissions. In the absence of such evidence thermal emission is assumed here for interpretation. Intensities, I, are usually expressed in brightness temperature, T_b, in radio astronomy using the Rayleigh-Jeans approximation for conversion

$$T_b = \frac{c^2 I}{2\nu^2 k_B} \,, \quad (3)$$

where ν is the observing frequency and k_B the Boltzmann constant. In isothermal black bodies T_b equals the kinetic temperature. The brightness temperature is the solution of the transfer equation

$$T_b = \int_0^\infty T_e e^{-\tau} \mathrm{d}\tau \,. \quad (4)$$

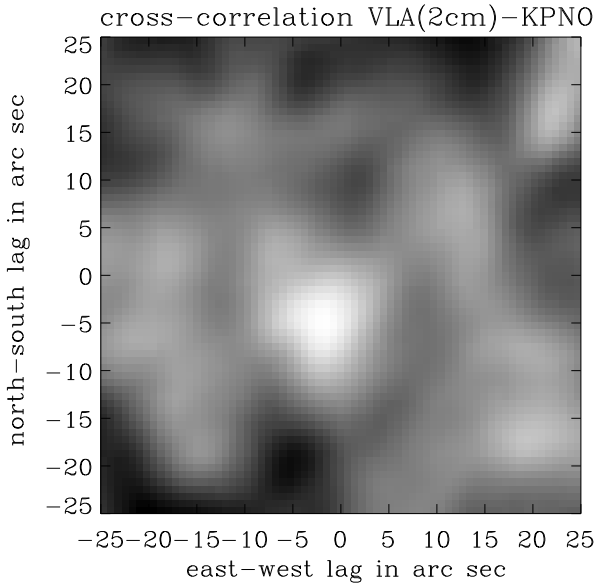

Fig. 6. Two-dimensional cross-correlation of the radio image observed by the VLA at 2cm and the absolute photospheric magnetic field (KPNO magnetogram). The selected field is the center part of the circular radio field of view (primary beam).

Neglecting the magnetic field, the optical depth of free-free emission is given by (e.g. Benz 1993)

$$\mathrm{d}\tau = \frac{0.01146 \ln \Lambda \; n_e^2}{(1 - 8.06 \cdot 10^7 n_e/\nu^2)^{1/2} \nu^2 T_e^{3/2}} \; ds \qquad (5)$$

The Gaunt factor, $\ln \Lambda$, is a slowly varying function of electron temperature, T_e, and density amounting to about 8 in the upper chromosphere.

Eqs. (4) and (5) indicate that the effect of a temperature increase on the radio intensity is model dependent. Models of the upper chromosphere and transition region are still vividly disputed (e.g. Zirin et al. 1991). Chiuderi Drago et al. (1983) find increasing radio brightness from the network center (Vernazza et al. 1981, VAL model B), average network (VAL model D) to network elements (VAL model F) similar to the observed relative values. We note, however, that the VAL models yield an absolute brightness temperature that grossly exceeds the observed values (Zirin et al. 1991, Bastian et al. 1996).

The following investigation is based on the models of Fontenla et al. (FAL, 1993) which agree reasonably well with radio observations (Bastian et al. 1996). The differences in total brightness due to the slightly non-vertical ray path are less than 3 percent. Nevertheless, models should only be taken as a qualitative guide. Fig. 7 indicates the altitude of origin of the three radio wavelengths for the model quiet Sun. The contribution of the corona to the 3.6 cm emission is 5-10%, and an order of magnitude less at 1.3 cm.

The average model is now disturbed to find the necessary deviations for the observed radio structures. In Fig. 8 the temperature and density of the whole atmosphere (FAL model C) were

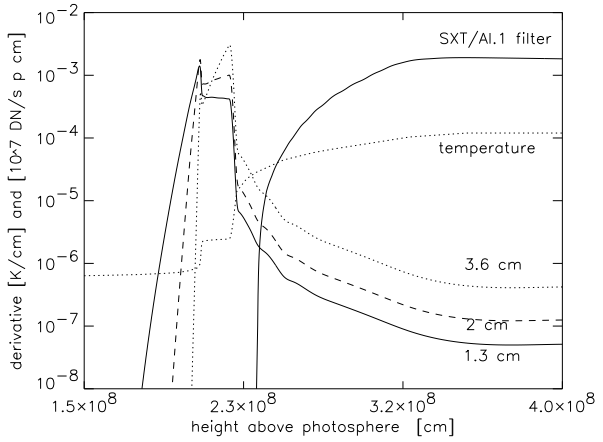

Fig. 7. Contribution to the radio brightness temperature per unit height in K/cm and contribution to the X-ray brightness (Al.1 filter) in units of 10^7 Data Numbers per second and pixel. The FAL model C (average quiet Sun) and the Baumbach-Allen corona model with $T_e = 1.3 \cdot 10^6$ K. The kinetic temperature is drawn for orientation on the same scale in units of 10^{10} K.

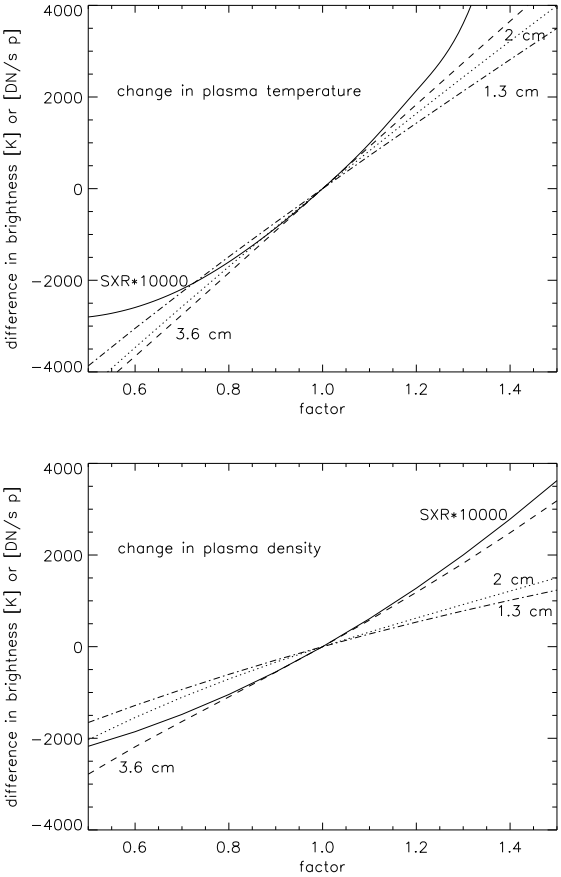

Fig. 8. The change of the brightness in radio [K] and X-rays [10^4 DN/s·p] relative to FAL model C caused by multiplying **a** the kinetic temperature or **b** the electron density by the factor given in the abscissa.

multiplied by constant factors. Although based on unconfirmed models, the Figs. 8a and b give an estimate on the changes in temperature and density necessary to interpret the observations. The observed variations in brightness temperature (Table 1) can roughly be related to these changes in temperature and/or density. For all the models we have tried, the calculations predict an increase in brightness temperature for higher plasma temperature and/or density. The largest effect for a given change is at the longest wavelength. This is consistent with the observed increase of the contrast with wavelength as indicated in Table 1.

In addition, the comparison of observations with models requires that the factorial change increases with wavelength. If for example the temperature is constant in FAL model C, an rms fluctuation in density by 10.2%, 17.6%, 16.4%, and 31.3% is necessary to produce the standard deviations in brightness of 1.3cm, 2.0cm, 3.6cm, and X-rays, as reported respectively in Table 1. These values correspond to half the average density enhancement between cell interior and network at the source heights of the various radiations. It is noted, however, that the quantitative results depend strongly on the chromospheric model. The VAL model, for example, requires a factor of two smaller fluctuations to account for the radio variations.

5. Conclusions

Two deep soft X-ray exposures of a quiet region of the solar corona have revealed considerable structure. Regions of enhanced X-ray emission are often between bipolar regions of the magnetic network. There is a significant correlation between the absolute magnetic field strength and X-ray emission.

The comparison with radio images at different wavelengths reveals a picture in which the correlation between magnetic network elements and enhanced emission is best for the shortest radio wavelength originating at the lowest altitude in the chromosphere. The correlation becomes weaker and the maxima of correlation are more displaced from zero lag at longer radio wavelengths. The correlation further decreases for X-rays, which originate entirely in the corona.

On the other hand, the ratio of the rms brightness variations to the mean brightness increases from small-wavelength radio images to X-ray images. Using the average brightness temperatures measured for the quiet Sun (Gary & Zirin 1988; Bastian et al. 1996), the standard deviations amount to 2.8% at 1.3cm, 4.5% at 2.0cm, and 5.8% at 3.6cm. They are similar to the X-ray brightness deviations of 5.7%.

The changes in correlation and standard deviations with height are consistent with the frequent observations of X-ray emitting structure between bipolar regions. It suggests a general scenario of magnetic fields deviating from vertical in the upper chromosphere. The structures of enhanced X-ray emission suggest that many of these fields are closed and return to the photosphere within the network.

Acknowledgements. We thank C. Keller and P. Bernasconi for helpful discussions. The *Yohkoh* mission of ISAS, Tokyo, was prepared and is operated by an international collaboration of Japanese, US and UK scientists under the support of ISAS, NASA, and SERC, respectively. The National Radio Astronomy Observatory is operated by Associated Universities, Inc., under cooperative agreement with the National Science Foundation. The Kitt Peak magnetogram was produced cooperatively by NSF/NOAO/NASA/GSFC, and NAOO/SEL. This work was supported by the Swiss National Science Foundation, grant Nr. 20-040 336.94.

References

Bastian T.S., 1994, ApJ 426, 774
Bastian T.S., Dulk G.A., Leblanc Y., 1996, ApJ, 473, in press.
Benz A.O., 1993, Plasma Astrophysics, Kluwer, Dordrecht, Holland
Chiuderi Drago F., Kundu M.R., Schmahl E.J. 1983, Solar Phys. 85, 237
Erskine F.T., Kundu M.R., 1982, Solar Phys. 76, 22l
Fontenla J.M., Avrett E.H., Loeser R., 1993, ApJ 406, 319 (FAL)
Fu Q., Kundu M.R., Schmahl E.J., 1987, Solar Phys. 108, 99
Gary D.E., Zirin H., 1988, ApJ 329, 991
Gary D.E., Zirin H., Wang H., 1990, ApJ 355, 321
Golub L., Krieger A.S., Silk J.K., Timothy A.F., Vaiana G.S., 1974, ApJ 189, L93
Gómez D.O., Martens P.C.H., Golub L., 1993, ApJ 405, 767
Habbal S.R., Harvey K.L., 1988, ApJ 326, 988
Habbal S.R., Ronau R.S., Withbroe G.L., Shevgaonkar R.K., Kundu M.R., 1986, ApJ 306, 740
Harvey K.L., 1985, Australian J. Phys. 38, 875
Kundu M.R., Rao A.P., Erskine F.T., Bregman J.D., 1979, ApJ 234, 1122
Kundu M.R., Schmahl E.J., Fu Q.-J., 1988, ApJ 325, 905
Kundu M.R., Shibasaki K., Enome S., Nitta N., 1994, ApJ 431, L155
Krucker S., Benz A.O., Acton L.W., Bastian T.S., 1997, ApJ, submitted
Nitta N., Bastian T. S., M. J. Aschwanden M. J., Harvey K. L., Strong K. T., 1992, PASP 44, L167
Tsuneta S. et al., 1991, Solar Phys. 136, 37
Vernazza J.F., Avrett E.H., Loeser R., 1981, ApJS 45, 635 (VAL)
Yoshida T., Tsuneta S., 1969, ApJ 459, 342
Zirin H., Baumert B.M., Hurford G.J., 1991, ApJ 370, 779